AGU PUBLICATIONS

Tectonics

RESEARCH ARTICLE
10.1002/2014TC003545

Key Points:
- Slow *S* wave speeds in Tibet require the presence of a few percent partial melt
- *S* wave anisotropy in Tibet requires subhorizontally oriented mica

Correspondence to:
B. R. Hacker,
hacker@geol.ucsb.edu

Citation:
Hacker, B. R., M. H. Ritzwoller, and J. Xie (2014), Partially melted, mica-bearing crust in Central Tibet, *Tectonics*, *33*, doi:10.1002/2014TC003545.

Received 29 JAN 2014
Accepted 7 MAY 2014
Accepted article online 8 JUL 2014

Partially melted, mica-bearing crust in Central Tibet

B. R. Hacker[1], M. H. Ritzwoller[2], and J. Xie[2]

[1]Earth Science, University of California, Santa Barbara, California, USA, [2]Department of Physics, University of Colorado Boulder, Boulder, Colorado, USA

Abstract Surface wave tomography shows that the central Tibetan Plateau (the Qiangtang block) is characterized by *S* wave speeds as slow as 3.3 km/s at depths from 20–25 km to 45–50 km and *S* wave radial anisotropy of at least 4% ($V_{SH} > V_{SV}$) that is stronger in the west than the east. The depth of the Curie temperature for magnetite inferred from satellite magnetic measurements, the depth of the α-β quartz transition inferred from V_P/V_S ratios, and the equilibration pressures and temperatures of xenoliths erupted from the middle to deep crust indicate that the Qiangtang crust is hot, reaching 1000°C at the Moho. This inferred thermal gradient crosses the dehydration melting solidi for crustal rocks at 20–30 km depth, implying the presence or former presence of melt in the Tibetan middle to deep crust. These temperatures do not require the wholesale breakdown of mica at these depths, because F and Ti can stabilize mica to at least 1300°C. Petrology suggests, then, that the Qiangtang middle to deep crust consists of a mica-bearing residue from which melt has been extracted or is being extracted. Wave speeds calculated for mica-bearing rocks with a subhorizontal to gently dipping foliation and 2% silicate melt are a good match to the wave speeds and anisotropy observed by seismology.

1. Introduction

Quantifying the temperature gradient, rheology, and volume of melt or fluid lies at the heart of resolving how the Tibetan Plateau (Figure 1) has evolved, including, for example, the rates and regions of large-scale crustal flow [*Bird*, 1991; *Clark and Royden*, 2000]. A large and growing body of evidence suggests that the middle crust of the plateau is exceptionally warm, probably ductile, and may contain partial melt or aqueous fluid. Some of this evidence is geographically localized—such as observations of low electrical resistivity in the middle to lower crust [e.g., *Unsworth et al*., 2005; *Bai et al*., 2010] and strong *P* to *S* conversion bright spots on active-source wide-angle reflection data that have been cited as indicating midcrustal melt or fluids [e.g., *Makovsky and Klemperer*, 1999; *Makovsky et al*., 1999]. Localized seismological evidence that points to a midcrustal low-velocity layer derives from surface wave dispersion, receiver function, and wide-angle reflection studies [e.g., *Kind et al*., 1996; *Cotte et al*., 1999; *Rapine et al*., 2003; *Mechie et al*., 2004; *Jiang et al*., 2006; *Xu et al*., 2007; *Caldwell et al*., 2009; *Guo et al*., 2009; *Li et al*., 2009; *Wang et al*., 2013; *Xu et al*., 2013b]. Other evidence, more broadly distributed across Tibet, includes the absence of middle to lower crustal earthquakes [e.g., *Chu et al*., 2009; *Sloan et al*., 2011], extensive Cenozoic volcanism [e.g., *Chung et al*., 2005], satellite magnetic anomalies consistent with a raised Curie isotherm [*Alsdorf and Nelson*, 1999], strong crustal attenuation [e.g., *Xie*, 2004; *Rai et al*., 2009; *Levshin et al*., 2010], pervasive slow speeds in seismological models of the middle crust [e.g., *Villaseñor et al*., 2001; *Shapiro and Ritzwoller*, 2002; *Yao et al*., 2008; *Acton et al*., 2010; *Yao et al*., 2010; *Jiang et al*., 2011; *Yang et al*., 2012], and strong midcrustal radial anisotropy [e.g., *Shapiro et al*., 2004; *Duret et al*., 2010; *Huang et al*., 2010; *Xie et al*., 2013].

The purpose of this paper is to test the hypothesis that partial melt exists pervasively in the middle crust across Tibet and to explain the origin of the strong midcrustal radial anisotropy. To make this assessment, we calculate wave speeds within the Tibetan crust based on mineral physical properties and petrological constraints and then compare these calculations to models of crustal shear wave speeds and radial anisotropy.

2. Seismological Observations

Seismological investigations of the Tibetan Plateau crust are now relatively numerous and have employed a range of techniques that reveal different aspects of the seismic characteristics of the plateau. The most notable discoveries include the following four. (1) Most of the reported V_P gradients increase

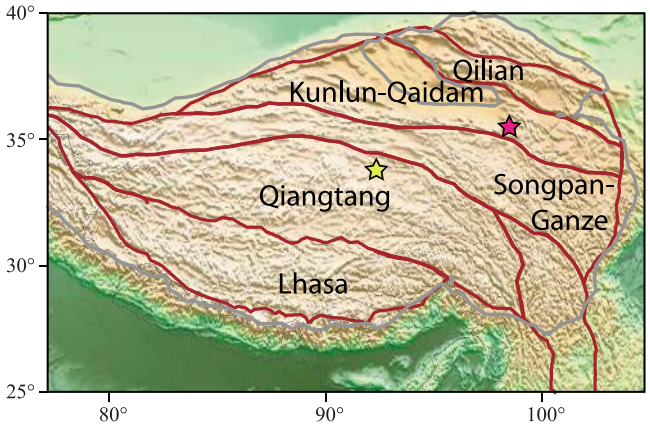

Figure 1. Major geologic units and topography of the Tibetan Plateau. Gray line marks 3 km elevation. Gold star marks the location of Figure 6 Qiangtang profile and xenolith eruption site; pink star is complementary site in Qaidam.

monotonically from ~6 km/s in the shallow crust to ~7 km/s in the deep crust, but at least two studies reported slow V_P layers at ~30 km depth in the Songpan-Ganze and Kunlun-Qaidam blocks [*Jiang et al.*, 2006; *Wang et al.*, 2013]. (2) Many of the reported V_S gradients increase monotonically downward from ~3.1 km/s to ~4.3 km/s. A majority of studies in the Qiangtang block, however, report slow, 3.2–3.4 km/s, layers at depths from 20–25 km to 45–50 km [*Vergne et al.*, 2002; *Rapine et al.*, 2003; *Mechie et al.*, 2004; *Duret et al.*, 2010; *Yang et al.*, 2012; *Xu et al.*, 2013b], and most studies of the Lhasa block show a similarly slow layer at 20–40 km depth. (3) The few studies of radial anisotropy from surface waves report that $V_{SH} > V_{SV}$ by up to 10% [*Chen et al.*, 2009; *Duret et al.*, 2010]. (4) Most studies of V_P/V_S have reported values for the entire crust of 1.73–1.78, but *Mechie et al.* [2004] reported V_P/V_S gradients within the Qiangtang block that reached values as low as 1.67–1.69 at ~15–20 km depth.

3. A Forward Model for the Seismic Properties of Tibet

The Tibetan Plateau is composed of continental blocks—e.g., the Lhasa, Qiangtang, Songpan-Ganze (or Bayan Har), and Kunlun-Qaidam blocks—sequentially rifted from Gondwana and accreted to the southern margin of Asia during the Mesozoic [*Yin and Harrison*, 2000; *DeCelles et al.*, 2002]. To interpret the seismic characteristics reported for the plateau, we calculate a forward model for the middle to lower crust of the Qiangtang block (henceforth Qiangtang). Qiangtang forms the heart of the plateau and has the best constrained thermal gradient and a reasonably well-known or inferred crustal section.

To create a forward model of isotropic wave speeds, we need to know the mineralogy, pressure, and temperature as a function of depth within the crust, and we must know the elastic properties of the constituent minerals. To calculate velocity anisotropy we need, in addition, to know the crystal-preferred orientations (CPOs) of the minerals in the rocks in a geographic reference frame. Unlike plutonic rocks that can form with isotropic fabrics, metasedimentary rocks contain subhorizontal stratigraphic layers and subhorizontally oriented micas grown from clays. Such rocks are expected to have elastic properties with approximately hexagonal symmetry and a subvertical, slow symmetry axis.

3.1. Rock Types Within Qiangtang

The minerals that are stable at different depths within Qiangtang are determined by rock type, pressure, and temperature. The rocks within Qiangtang are incompletely known because of limited exhumation but inferred to be predominantly Carboniferous-Jurassic shallow marine clastic rocks overlying a crystalline, chiefly quartzofeldspathic basement derived from underthrust Lhasa block and Songpan-Ganzi block [*Kapp et al.*, 2003; *Guynn et al.*, 2006; *Pullen et al.*, 2010]. Correlated, more deeply exposed, units in the Pamir [*Schwab et al.*, 2004; *Schmidt et al.*, 2011], west of Tibet, underscore the interpretation that Qiangtang is made of a metasedimentary section overlying crystalline basement. Xenoliths erupted at several localities in central Qiangtang indicate that the middle crust includes intermediate-mafic granulites (49–56 wt % SiO_2) and metasedimentary granulites (50–70 wt % SiO_2) [*Deng*, 1996; *Hacker et al.*, 2000; *Ding et al.*, 2007]. The granulites reached temperatures of 900–1000°C by 28 Ma [*Ding et al.*, 2007] and were heated even further at 3 Ma [*Hacker et al.*, 2000].

Table 1. Compositions of Model Rocks

wt %	Basalt[a]	Pelite[b]	Wacke[c]	Tonalite[d]	Marble
SiO_2	50.2	64.4	70.4	60.8	
TiO_2	1.9	0.8	0.7	0.9	
Al_2O_3	15	18.1	13.1	16.9	
FeO	9.1	6.4	4.9	6	
MgO	7.4	2.4	2.4	2.7	
CaO	8.6	1.5	1.7	6.3	56
Na_2O	3.8	1.7	3	3.8	
K_2O	4	2.6	2.4	2.5	
H_2O	0.5	0.8	1.1	0.7	
CO_2	0	0	0	0	44

[a]Median of Tibetan basalts studied by *Ding et al*. [2003] and *Turner et al*. [1996].
[b]*Vielzeuf and Holloway* [1988].
[c]*Montel and Vielzeuf* [1997].
[d]*Patiño Douce* [2005].

3.2. Mineralogy Within Qiangtang

We model the mineralogy of Qiangtang using a range of rock types typical of the crust: pelite, wacke, marble, tonalite, and a potassic basalt (Table 1). We calculate the subsolidus mineralogy as a function of pressure and temperature (PT) using *Perple_X* [*Connolly and Petrini*, 2002] and the activity models listed in Table 2. Melt activity models for crustal rocks have relatively limited applicability, so we interpolate and extrapolate the hypersolidus mineralogy from the results of experiments on pelite, wacke, tonalite, and amphibolite [*Vielzeuf and Holloway*, 1988; *Skjerlie and Johnston*, 1993; *Sen and Dunn*, 1994; *Rapp and Watson*, 1995; *Montel and Vielzeuf*, 1997; *Patiño Douce*, 2005]. We consider only dehydration melting, excluding the possibility of H_2O-saturated melting. Because phase transformations in Earth are inhibited during cooling, such that metastable mineral assemblages are common in rocks, we use the mineral assemblage calculated for 500°C at all lower temperatures; this is not a significant limitation because the seismic properties of the crust at these temperatures are strongly influenced by porosity, which we also ignore.

3.3. Temperature and Pressure Within Qiangtang

We calculate density within Qiangtang from an empirical relationship with V_P (after that of *Birch* [1961]) defined by our literature survey: density (g/cm^3) = 0.1 + 0.43 V_P (km/s). We use the average of the V_P gradients reported for Qiangtang by *Mechie et al*. [2004] and *Galvé et al*. [2002] as input. This means that the pressure at the ~65 km deep Moho [*Mechie et al*., 2004; *Li et al*., 2006; *Yang et al*., 2012] is ~1.8 GPa (Figure 2a).

There are several constraints on the temperature gradient within Qiangtang (Figure 2a): (i) an inferred depth of 15 ± 5 km for the 550°C Curie temperature for magnetite [*Alsdorf and Nelson*, 1999], (ii) an inferred depth of 18 km for the ~700°C α-β quartz transition [*Mechie et al*., 2004], and (iii) a Moho temperature of ~1000°C inferred from the ~7.9–8.0 km/s Pn speed reported by *McNamara et al*. [1997] and *Liang and Song*, 2006.

Table 2. Perple_X Activity Models

Mineral	Model	Reference
Biotite	Bio(TCC)	*Tajcmanová et al*. [2009]
Chlorite	Chl(HP)	*Holland and Powell* [1998]
Feldspar	feldspar	*Fuhrman and Lindsley* [1988]
Amphibole	GlTrTsPg	*Wei and Powell* [2003]
Garnet	Gt(HP)	*Holland and Powell* [1998]
Ilmenite	Ilm(WPH)	*White et al*. [2000]
White mica	Mica(CHA)	*Coggon and Holland* [2002] and *Auzanneau et al*. [2010]
Olivine	O(HP)	*Holland and Powell* [1998]
Clinopyroxene	Omph(HP)	*Holland and Powell* [1998]
Orthopyroxene	Opx(HP)	*Holland and Powell* [1998]
Alkali feldspar	San(TH)	*Thompson and Hovis* [1979]

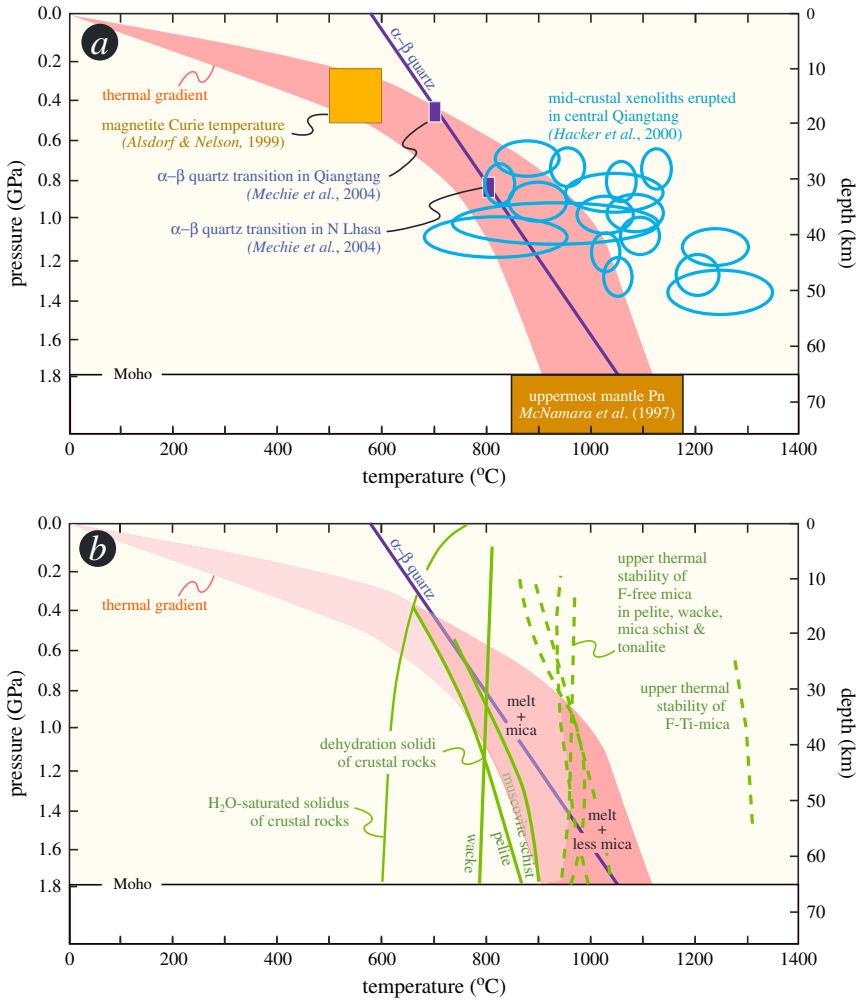

Figure 2. (a) The temperature (pink) beneath the central Tibetan Plateau is constrained by the surface temperature, the depth of the Curie temperature for magnetite (yellow) inferred from satellite magnetic measurements, the depth of the α-β quartz transition (navy) inferred from Poisson's ratios [*Mechie et al.*, 2004], the PT equilibration conditions of xenoliths (cyan), and Pn wave speeds (brown). (b) The temperature exceeds the solidi (solid green lines) for crustal rocks [*Vielzeuf and Montel*, 1994; *Patiño Douce and Beard*, 1995; *Patiño Douce and McCarthy*, 1998; *Patiño Douce*, 2005] beyond depths of 20–30 km, implying the presence or former presence of melt in the middle to deep crust. Micas remain stable to ~1000°C in crustal rocks (dashed green lines) and considerably higher if they contain fluorine and titanium [*Dooley and Patino Douce*, 1996], like the Tibetan xenoliths, implying the presence of mica in the middle to deep crust.

Thisis similar to the temperature gradient assumed for Qiangtang in a recent thermal model [*Craig et al.*, 2012] in which the high crustal temperatures are produced by in situ radiogenic heating. Xenoliths erupted in central Qiangtang provide additional insight into the thermal structure earlier in the Cenozoic. Mineral compositions indicate equilibration temperatures of ~900–1000°C at 30–40 km depth prior to 28 Ma and subsequent heating to 1100–1200°C by 3 Ma [*Hacker et al.*, 2000; *Ding et al.*, 2007]; whether the latter was the result of magmatic heating alone is unknown.

Three important petrological conclusions derive from this temperature gradient (Figure 2b).

1. The H_2O-saturated solidi for crustal rocks [*Ebadi and Johannes*, 1991; *Nichols et al.*, 1994] are exceeded at depths of 15–25 km. If the Tibetan crust were being fluxed with H_2O, all of it below a depth of ~15–25 km would have melted or should still be partially molten; H_2O-fluxed melting is generally considered implausible, however, because of the sheer amount of H_2O required.
2. The mica-dehydration solidi for crustal rocks are exceeded by the model geotherm at depths > ~20–30 km, requiring that dehydration melting either has taken place or is taking place in the middle to lower crust.

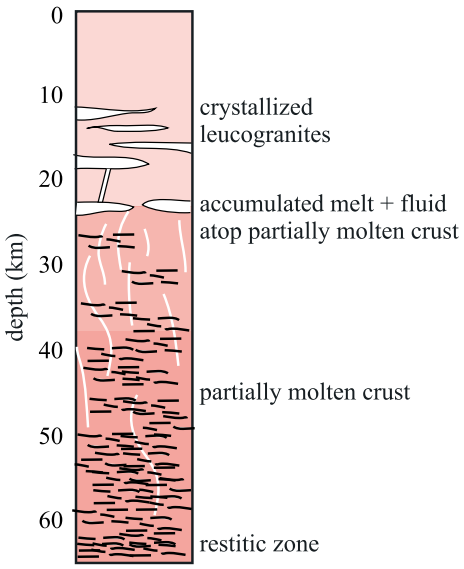

Figure 3. The Qiangtang block is actively melting—or has previously melted—at depths >20–30 km. The most melt is being produced at depths of 20–30 km where rising isotherms encounter unmelted rock, but small amounts of melt are being produced at greater depths in previously depleted rock where the temperature is rising. The melt accumulates atop the melted zone and then propagates in dikes to 10–20 km depth where it crystallizes. At depths >20–30 km, the crust is a mixture of (i) partially melted rock, (ii) formerly melted and now-depleted rock (restite), or (iii) unmelted rock; the specific state depends on pressure temperature, volatile content, and rock composition [after *Scaillet and Searle*, 2006].

The volume of such melts is expected to be large: experiments indicate that dehydration melting of pelite and wacke yield melt fractions of 20–60% at temperatures of 900°C (summary in *Hacker et al*. [2011]).

3. Mica and hornblende are stable above the dehydration solidus to at least ~950°C (30–40 km), and fluorine and titanium stabilize hornblende to nearly 1100°C at 1 GPa [*Holloway and Ford*, 1975] and stabilize mica to even higher temperature (Figure 2b) [*Holloway and Ford*, 1975; *Dooley and Patino Douce*, 1996]. Mica and hornblende should therefore be stable in rocks of appropriate composition at all depths within the plateau. These conclusions are supported by the presence of high-fluorine, high-titanium mica, and hornblende in xenoliths erupted from the midcrust of Qiangtang [*Hacker et al*., 2000].

3.4. Has the Plateau Melted or is the Plateau Molten?

If the thermal gradient in Figure 2a is correct, rocks at depths > ~ 20–30 km should be actively melting or have undergone melting in the past (Figure 2b). At least the upper half of the Qiangtang crust is composed of metasedimentary rocks that were only weakly metamorphosed prior to the Cenozoic; this means that they would have been fertile and able to produce significant volumes of melt when heated during the Cenozoic. Thus, we conclude, like others before us (see section 1), that petrology dictates that melt and fluid are present—or were once present—within the plateau crust at depths >20–30 km. Wherever the Tibetan crust is heating, melt may be being produced; wherever the crust is cooling, melt is not being produced unless H_2O is being added.

The conclusion that the entire Tibetan Plateau crust below a depth of 20–30 km is either melting or has melted stands in contrast to the feeble expression of Cenozoic silicic magmatism on the plateau [*Chung et al*., 2005; *Wang et al*., 2012]. There are (at least) two possible resolutions to this conundrum. Perhaps the simplest is that the crust at >20–30 km depth was depleted during an earlier melting event, such that late Cenozoic heating produced only small amounts of melt. *Guillot and Replumaz* [2013] have argued that early Cenozoic slab breakoff events produced widespread granulite formation and melting of the Tibetan lower crust. Alternatively, one might argue that dehydration melts of crustal rocks do not often reach the surface because of high viscosity or because they are produced in small batches that rise and freeze without erupting. Perhaps the best example of this is the abundant High Himalayan leucogranites, which are chiefly sills up to 10 km thick and 60 km wide [*LeFort*, 1981; *Searle*, 1999; *Searle et al*., 2010]. These crustally derived melts were generated in small volumes at midcrustal depths [*Guillot et al*., 1995] and migrated upward as much as 10 km [*Searle et al*., 2010] and laterally as much as 50–100 km [*Scaillet and Searle*, 2006], and yet there is little sign that they ever rose higher than ~10 km beneath the surface or that they erupted. Therefore, the Qiangtang crust may look much like Figure 3 [after *Scaillet and Searle*, 2006], with minor active melting in a previously depleted middle to deep(?) crust capped by a zone of accumulated melt and hydrous fluid that feeds small-volume magmas upward to freeze in the shallow crust and underlain by a refractory lower crust.

3.5. Calculated Wave Speeds

We calculate isotropic wave speeds from rock mineralogy as a function of pressure and temperature, using the algorithm of *Hacker and Abers* [2004] modified to account for the elastic properties of quartz

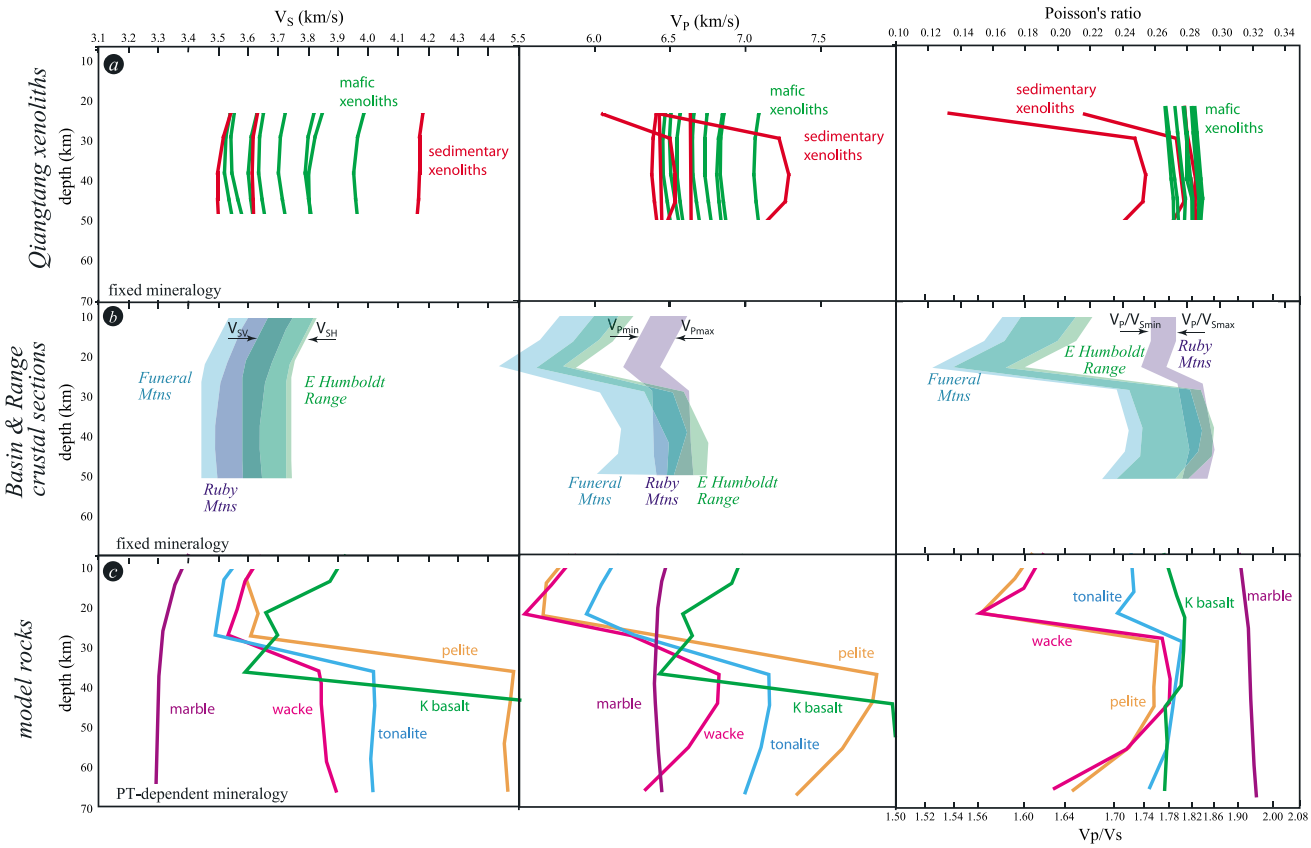

Figure 4. Wave speeds calculated for (a) Tibetan xenoliths, (b) crustal sections, and (c) model rocks, given the Qiangtang PT gradient in Figure 2. Figure 4a shows xenolith speeds calculated from observed rock abundances and mineral modes. Figure 4b shows crustal section speeds calculated from observed rock abundances, CPOs, mineral modes, and compositions. Width of colored bar shows range in wave speeds or ratios for fastest and slowest directions of wave propagation (arrows mark these values for the Ruby Mountains section as an example). Figure 4c shows model rock speeds calculated from mineral modes and compositions that vary as a function of PT. The sharp decreases in wave speed at the base of the crust are caused by the modeled PT gradient crossing back into the alpha quartz stability field.

subsequently reported by *Ohno et al.* [2006] and *Lakshtanov et al.* [2007]; melt, fluid, and porosity were ignored. This was done for the model compositions listed above (pelite, wacke, marble, tonalite, and potassic basalt) and for compositions of actual mafic and metasedimentary xenoliths from Tibet (Figure 4).

Velocity *anisotropy* was calculated (Figure 4b) for three crustal sections studied in the Basin and Range Province of North America by *Erdman et al.* [2013] that are composed of rock types similar to those inferred for Qiangtang. The velocity anisotropy of individual rocks was calculated by using the Christoffel equation to calculate the elastic properties of each mineral from the STP (standard temperature and pressure) single-crystal elastic constants (C_{ij}) and a CPO typical of each mineral (Table 3) and then

Table 3. Sources of Data for Anisotropy Calculations[a]

Mineral	Stiffness Matrix, C_{ij}	CPO From Sample	Slip System
Biotite	*Aleksandrov and Ryzhova* [1961b]	9804e of *Erdman et al.* [2013]	[uv0](001)
Muscovite	*Vaughan and Guggenheim* [1986]	MC5 of *Erdman et al.* [2013]	[uv0](001)
Amphibole	*Aleksandrov and Ryzhova* [1961a]	RM26 of *Erdman et al.* [2013]	[001]{1–20}
α quartz	*Lakshtanov et al.* [2007]	Y1612D of *Barth et al.* [2010]	[001](100)
Calcite	*Chen et al.* [2001]	9804f of *Erdman et al.* [2013]	<11–20>{0001}
Plagioclase	*Aleksandrov et al.* [1974]	9804e of *Erdman et al.* [2013]	[001](010)
Garnet	*Babuska et al.* [1978]	MC3 of *Erdman et al.* [2013]	isotropic

[a]For each mineral is listed (i) the source of the stiffness matrix, (ii) the sample from which the representative CPO was taken, and (iii) the main slip system inferred to be responsible for the CPO.

computing a Voigt-Reuss-Hill average of the elastic properties of the minerals in proportion to their modal abundance. This STP anisotropy was then scaled to high P and T using the ratio of the isotropic STP and isotropic high-PT values calculated via Hacker and Abers. It would be preferable to use high-pressure and high-temperature C_{ij}, but these are not available for any of the minerals of interest. The anisotropy of the crustal section was computed by averaging the individual rock C_{ij} in proportion to rock abundance [*Erdman et al*., 2013].

Note that only the mineralogy of the model rock types (Figure 4c) was allowed to vary as a function of PT. This has the advantage that the computed wave speeds reflect thermodynamic equilibrium at PT but the disadvantage that the Tibetan crust is not composed of single rock types; interpolation among the different compositions is therefore required. In contrast, the observed mineral modes and compositions of the Qiangtang xenoliths (Figure 4a) and the Basin and Range sections (Figure 4b) were held invariant at all PT. This has the advantage that the computed wave speeds reflect actual xenoliths from the Tibetan middle crust and actual lithologically diverse crustal sections, but the disadvantage that the calculated wave speeds are likely only to match a limited PT range; extrapolation to other PT is required. Because the Qiangtang metasedimentary xenoliths have had considerable melt extraction—and are therefore fast, even though felsic [*Hacker et al*., 2000]—whereas the Basin and Range crustal sections have had minimal melt extracted, one would expect that the xenoliths might be a better fit to the Tibetan middle to lower crust and that the crustal sections might be a better fit to the upper crust. Wave speeds were not calculated for the upper 10 km because the seismic properties of the uppermost crust are strongly influenced by porosity.

4. Comparison of Calculated and Observed Wave Speeds

4.1. Observed *S* Wave Speeds

Many V_S measurements have been reported for the Tibetan crust. Each of these data sets can be considered individually, but to make a uniform map of V_S across Tibet, we combine the recent models of crustal V_{SV} across all of Tibet by *Yang et al*. [2012] and of V_{SV}, V_{SH}, and V_S across eastern Tibet by *Xie et al*. [2013] (Figure 5). From this we construct maps of the estimated isotropic shear wave speed and the amplitude of shear wave radial anisotropy $((V_{SH} - V_{SV})/V_S)$ at 30 km depth in the middle crust across all of Tibet (Figures 5d–5f). These maps are then used to constrain the spatial variation of shear velocity structure in the middle crust and to identify a typical crustal shear velocity profile.

Yang et al. [2012] applied standard ambient noise data processing procedures [e.g., *Bensen et al*., 2007; *Yang et al*., 2010] to continuous vertical component data recorded at about 600 stations in Tibet and surrounding areas. They used data from 2003 to 2009 to produce ~50,000 high-quality interstation Rayleigh wave cross correlations on which phase-velocity measurements between 8 and 65 s period were obtained. These data resulted in a crustal V_{SV} model across all of Tibet and parts of the surrounding region.

Most surface wave studies of Tibet have been based exclusively on Rayleigh waves and therefore on inferred V_{SV}. It is preferable, however, to investigate the likelihood of partial melt in the Tibetan middle crust using isotropic shear wave speed, V_S, rather than V_{SV} for two reasons. (1) Partial melt—if it exists—should produce a signature visible in V_{SV} and V_{SH}, and thus V_S; slow V_{SV} could be produced by features other than melt—such as subhorizontal mica. (2) V_{SV} determined from Rayleigh waves alone tends to be affected by vertical oscillations; the introduction of Love waves not only allows for the simultaneous estimation of V_{SH} (and therefore V_S) but also stabilizes the inference of V_{SV} by making it less prone to vertical oscillations. The simultaneous observation of V_{SV} and V_{SH} also allows estimation of radial anisotropy—complementary evidence to constrain the physical state of the middle crust.

Xie et al. [2013] extended the analysis of *Yang et al*. [2012] to Love waves and produced Love wave phase speed measurements from 8 to 44 s period. Because Love waves are generally harder to observe than Rayleigh waves, the study of Xie et al. was restricted to the area of good station coverage in eastern Tibet—a subset of the region studied by Yang et al. In eastern Tibet, Xie et al. produced a model of both V_{SV} and V_{SH} and computed isotropic shear wave speed, V_S, via a Voigt average: $V_S = ((2\ V_{SV}^2 + V_{SH}^2)/3)^{1/2}$ [e.g., *Babuška and Cara*, 1991].

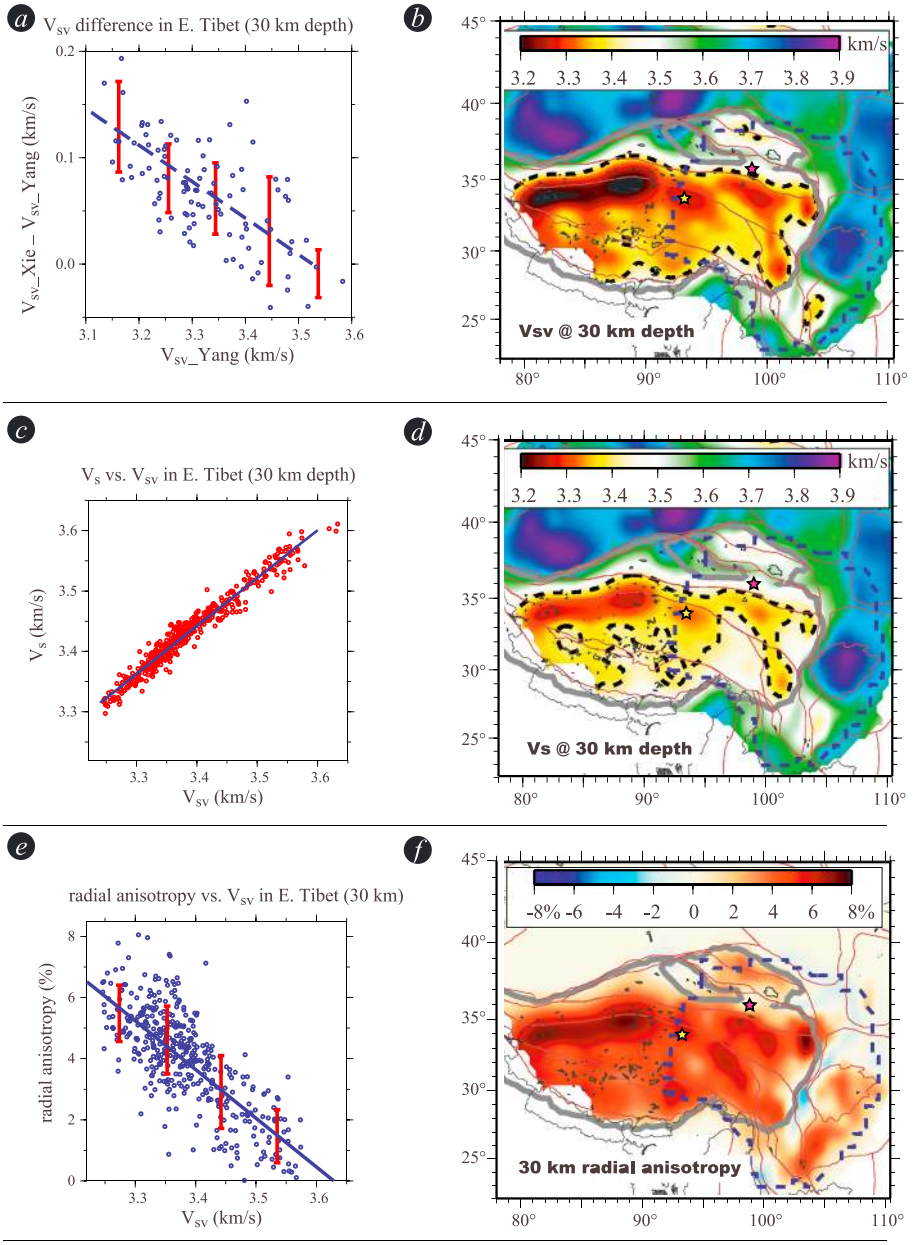

Figure 5. V_{SV}, V_S, and radial anisotropy maps for Tibet. Bold gray line in maps marks 3 km elevation. Gold star marks the location of Figure 6 Qiangtang profile and xenolith eruption site; red star is complementary site in Qaidam. (a) Correlation between V_{SV} determined at 30 km depth in the studies of *Yang et al.* [2012] and *Xie et al.* [2013] plotted as standard deviations of the difference. Positive values indicate V_{SV} from Yang et al. lower than V_{SV} from Xie et al. The blue dashed line indicates the correction applied to produce the revised V_{SV} values of Yang et al. plotted in Figure 5b. (b) Merged V_{SV} map for Tibet produced from correlation in Figure 5a. Values within blue dashed line from Xie et al.; remainder are revised V_{SV} values from Yang et al.. The dashed black line is the contour of 3.4 km/s for V_{SV}. (c) Correlation between V_S and V_{SV} in model of Xie et al. (d) Merged V_S map for Tibet produced from correlation in Figure 5c. Values within blue dashed line are from Xie et al.; remainder are from Yang et al. converted to V_{SV} using the line in Figure 5c. The dashed black line is the 3.4 km/s contour. (e) Correlation between V_{SV} and radial anisotropy $((V_{SH} - V_{SV})/Vs)$ in eastern Tibet in the model of *Xie et al.* [2013] plotted as standard deviations in bins of V_{SV}. (f) Merged radial anisotropy $(\gamma = (V_{SH} - V_{SV})/V_S)$ map for Tibet produced from correlation in Figure 5e. Values within blue dashed line from Xie et al.; remainder are V_{SV} from *Yang et al.* [2012] converted to radial anisotropy using line in Figure 5e. Regions outside Tibet appear to be isotropic, but no information exists about anisotropy there. (Note: because the model of Xie et al. is on a 0.5° × 0.5° grid whereas that of Yang et al. is on a 1° × 1° grid, there are more data in Figures 5c and 5e than in Figure 5a.)

4.2. Merging the Yang Et Al. and Xie Et Al. Models

Because the V_{SV} models of Yang et al. and Xie et al. overlap in eastern Tibet, a straightforward comparison of both is possible. Figure 5a summarizes this comparison, presenting the average difference (and standard deviations) between V_{SV} in the two models at 30 km depth across eastern Tibet. The difference between the models is largest for the slowest V_{SV} and reduces approximately linearly for larger V_{SV}, such that there is no difference above 3.53 km/s. Thus, to reconcile the Yang et al. and Xie et al. models for eastern Tibet, a correction must be applied to the model of Yang et al. In principle, such a correction could be applied at all crustal depths, but this is difficult because of differences in crustal thicknesses and variations in sedimentary cover. For this reason, we correct Yang et al.'s model only at 30 km depth and consider the variability in crustal structure across Tibet only at this depth. Assuming that this difference in V_{SV} between the models exists across all of Tibet, we produce a single V_{SV} model for all of Tibet at 30 km depth (Figure 5b) by subtracting the value from the fit line in Figure 5a to the V_{SV} model of Yang et al. and combine this with the V_{SV} model of Xie et al. to achieve the result presented in Figure 5b. The average value of V_{SV} within the 3.4 km/s contour (dashed black line) is 3.31 km/s, with a minimum of 3.13 km/s in the northern Qiangtang terrane of western Tibet.

4.3. Converting From V_{SV} to V_S

As noted above, V_S is preferable to V_{SV} when assessing whether slow wave speeds might result from partial melt. V_S and V_{SV} are well correlated in the model of Xie et al. for eastern Tibet (Figure 5c). If we assume that this linear relationship also holds across western Tibet, we can use the revised V_{SV} from Yang et al.'s model to calculate V_S in western Tibet. When merged with the V_S model of Xie et al. in eastern Tibet, we obtain a model of V_S at 30 km depth across all of Tibet (Figure 5d). The average value of V_S in Tibet (within the dashed black contour in Figure 5b) is 3.37 km/s, with values ranging between 3.22 km/s and 3.46 km/s.

4.4. Radial Anisotropy

There is also a correlation between V_{SV} and radial anisotropy, $\gamma = (V_{SH} - V_{SV})/V_S$, at 30 km depth in the Xie et al. model across eastern Tibet (Figure 5e). Assuming again that this correlation holds in western Tibet, we estimate midcrustal radial anisotropy (Figure 5f) by converting the revised V_{SV} values at 30 km depth from the model of Yang et al. to radial anisotropy and merging them with estimates of radial anisotropy from Xie et al. Radial anisotropy at 30 km depth is fairly homogeneous across Tibet, with an average of 5.1% and values ranging between ~1% and 8%; the larger values are in western Tibet.

4.5. Summary of the New V_S and Anisotropy Model of Tibet

There are three robust large-scale features of isotropic shear velocity V_S and radial anisotropy at 30 km depth worthy of note (Figures 5d and 5f). (1) Midcrustal V_S is slower across all of Tibet than in surrounding areas: much of Tibet, shown by the dashed black line in Figure 5d, has V_S below 3.4 km/s. (2) V_S is slower on average in western than in eastern Tibet. (3) Radial anisotropy is stronger in western than eastern Tibet. (4) A fourth observation is less robust: the slowest midcrustal V_S values (as low as 3.22 km/s) and strongest radial anisotropy (as strong as 8%) lie in northwestern Tibet in the Qiangtang terrane, south of the Tarim Basin. However, as discussed by Yang et al., this area is the least well-resolved part of Tibet and this feature has larger uncertainties than others across the map. Further observational efforts are needed to confirm or falsify these values.

4.6. Typical *S* Wave Speed Profile for Tibet

The calculations illustrated in Figure 5 can also be used to construct a vertical profile of V_{SH}, V_{SV}, and V_S that might be typical of the Tibetan crust. The western part of the study region of Xie et al. in the Qiangtang terrane is intermediate between slower and more anisotropic western Tibet and faster, less isotropic eastern Tibet (Figure 5). As an example of a more or less typical profile for Tibet, Figure 6b presents the model of Xie et al. for a point in the Qiangtang terrane of central Tibet (93°E, 34°N; shown with the yellow stars in Figures 1 and 5). The three model corridors (V_{SH}, V_{SV}, and V_S) represent 1 standard deviation about the mean of the estimated posterior distribution at each depth from the Bayesian Monte Carlo inversion of the Rayleigh and Love wave data shown in Figure 5a.

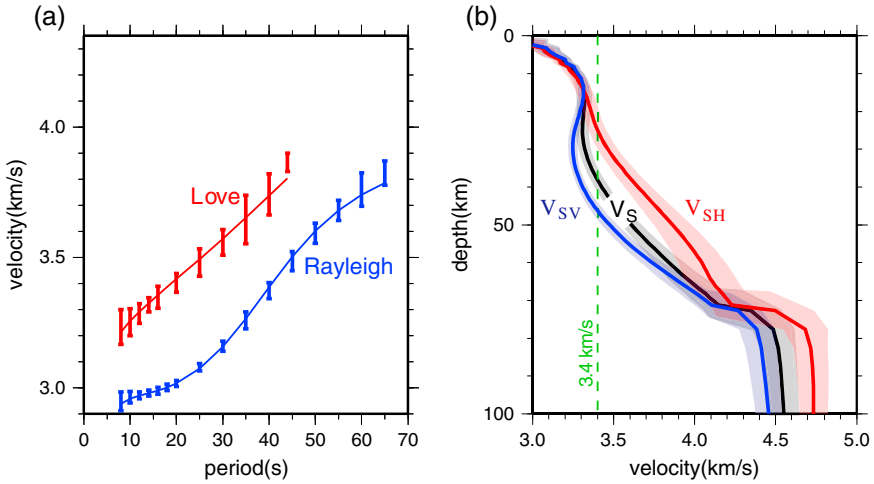

Figure 6. Example dispersion curves and estimated V_{SH}, V_{SV}, and V_S at the point in the Qiangtang terrane (93°E, 34°N) of Tibet identified by the gold star in Figure 5, which we take as a structurally typical point in Tibet. (a) Local Rayleigh and Love wave phase speed curves with 1 standard deviation (1σ) error bars. Predictions from the average of the anisotropic model distribution in Figure 6b are shown as solid lines. (b) Inversion result with the average of each ensemble plotted with bold lines and 1 standard deviation (1σ) model distributions shown with pale colors. Significant positive radial anisotropy between 20 and 50 km depth exists at this location.

A midcrustal low-velocity zone is evident in V_{SV} but not in V_{SH} at this point, a feature that is common across Tibet. At 30 km depth at this location, the mean V_{SV} is ~3.25 km/s, whereas it is ~3.47 km/s for V_{SH} and 3.32 km/s for *Vs*. Radial anisotropy at this point is ~6.6%. Although this is slightly slower and more anisotropic than average across Tibet, we use this as a typical profile for Tibet because this location is near the eruption site of the xenoliths studied by *Hacker et al.* [2000] and presented in Figure 4.

In closing, the radial anisotropy shown in Figure 6b that we take as more or less typical for Tibet is quite strong. It is clear from this that before interpreting shear wave speeds in terms of the potential existence of partial melt, one must first clarify which shear wave speed is to be cited. We focus interpretation on *Vs*, the isotropic shear wave speed, which is intermediate between V_{SH} and V_{SV}, and not on V_{SV} as so many other studies have done previously.

4.7. Comparison of Calculated and Observed Wave Speeds

In Figures 7a–7c, we interpret the V_S wave speed profile of Figure 6b—and, by implication, the rest of Tibet—by comparing the profile to our wave speeds calculated in Figure 4. Some of the Tibetan mafic and metasedimentary xenoliths have calculated V_S (Figure 7a) that match the observed V_S at depths of 40–50 km, reinforcing the conclusion that the xenoliths may be representative of the middle to lower Tibetan crust [*Hacker et al.*, 2000]. None of the xenoliths are a good match to the slow V_S observed at depths shallower than 40 km, however, in keeping with the expectation that the shallower crust is of lower metamorphic grade. Among the model rock compositions (Figure 7b), only marble yields calculated V_S close to the measured speeds at ≤30 km depth; pelite and wacke are expected to be present at these depths but have calculated V_S that are much faster than observed. At depths >30 km, mixtures of marble with subequal amounts of wacke or tonalite could match V_S, but pelite and basalt are calculated to be much too fast. The three crustal sections from the Basin and Range (Figure 7c) have V_S wave speeds similar to the observed V_{SH} at ~30–50 km depth, but none of them come close to the slow V_{SV} observed at shallower depths.

Figures 7d–7f show a similar comparison for a point in Qaidam (red star in Figures 1 and 5). At this location, there is no radial anisotropy in V_S. Unlike the Qiangtang section, the Qaidam section is reasonably well matched by some of the Tibetan xenoliths at depths of 20–50 km (Figure 7d), by a mixture of marble with subequal amounts of wacke or tonalite (Figure 7e), and by the Basin and Range crustal sections (Figure 7f).

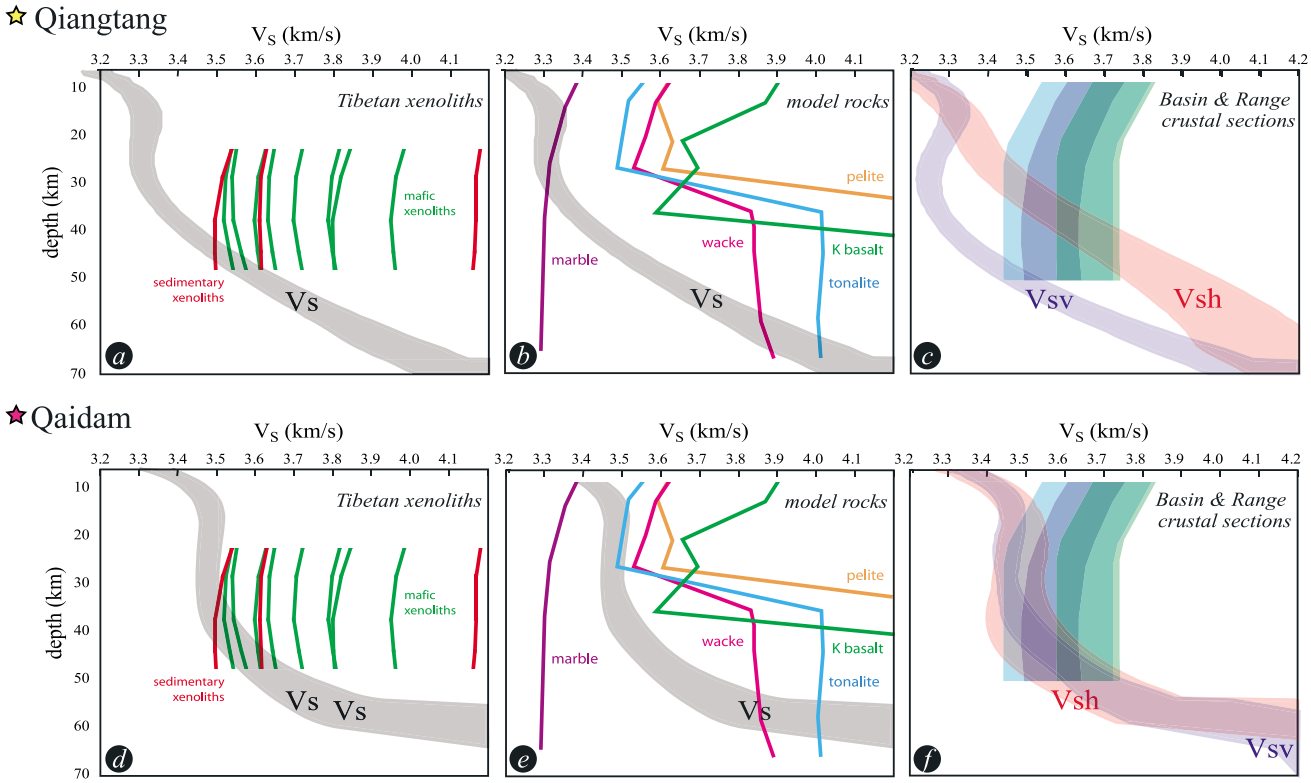

Figure 7. The observed central Qiangtang V_S wave speeds are not matched by wave speeds calculated for (a) Tibetan xenoliths, (b) model rocks, or (c) crustal sections. This mismatch suggests the presence of melt. In contrast, the observed V_S wave speeds for Qaidam are much more isotropic and nearly matched by wave speeds calculated for (d) Tibetan xenoliths, (e) model rocks, and (f) crustal sections. This match suggests the absence of melt beneath Qaidam.

In summary, the *S* wave speeds observed for Qiangtang can only be matched at depths <40 km by marble; the V_P/V_S ratio for Qiangtang, however, rules out the presence of marble, requiring another explanation for the slow Qiangtang *S* wave speeds. In contrast, the V_S observed for Qaidam is well matched by typical crustal rocks and no special explanation is required.

5. Comparison of Calculated and Observed V_P

There are relatively few V_P data for the Tibetan crust and only two studies for Qiangtang [*Mechie et al.*, 2004; *Galvé et al.*, 2006]. Our different types of isotropic V_P calculations can be compared with the two Qiangtang studies (Figure 8). The wave speeds for the xenoliths are equal to or faster than the measured V_P; the

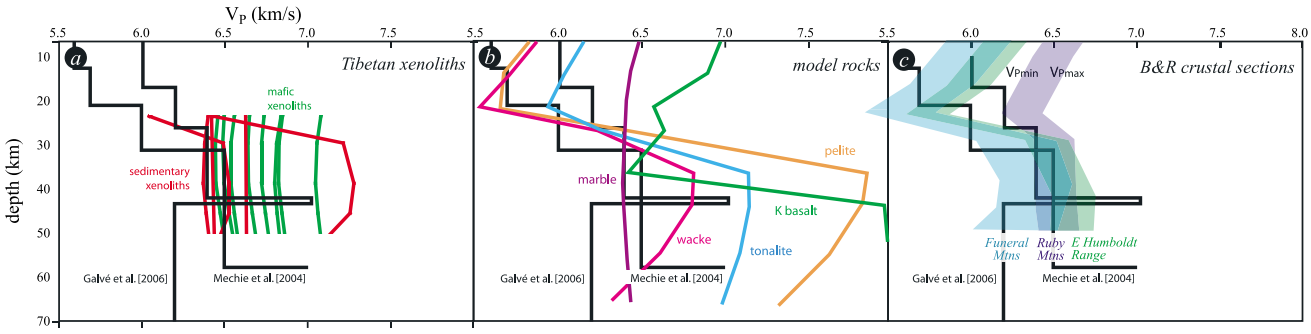

Figure 8. Observed V_P compared to V_P calculated for (a) Tibetan xenoliths, (b) model rocks, and (c) crustal sections. The correspondence is good for some metasedimentary xenoliths, for model quartzofeldspathic rocks at ≤30 km, for marble at ≥30 km, and for the Basin and Range crustal sections at all depths. Width of colored bar in Figure 8c shows range in V_P for different directions of wave propagation.

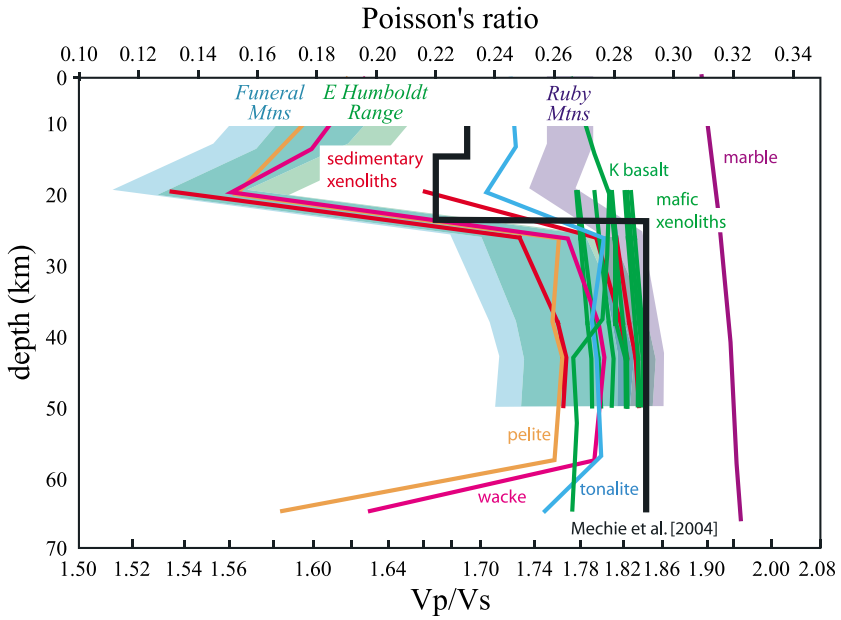

Figure 9. Observed V_P/V_S compared to V_P/V_S calculated for Tibetan xenoliths, model rocks, and crustal sections. The low V_P/V_S at ~20 km depth requires the presence of quartz-rich metasedimentary rock. Xenolith and crustal section speeds calculated from observed rock abundances, CPOs, mineral modes and compositions. Width of colored bar for crustal sections shows range in V_P/V_S for different directions of wave propagation. Model rock mineral modes and compositions vary as a function of PT.

metasedimentary xenoliths are a better fit, commensurate with a metasedimentary crust (Figure 8a). Among the model rock compositions, any one of the quartzofeldspathic rocks is a good match for the upper 30 km, and marble is a good match for depths ≥30 km (Figure 8b), although marble combined with any other rock type is not. For the Basin and Range crustal sections (Figure 8c shows the anisotropy in V_P), both of the quartz-rich Funeral Mountains and E Humboldt Range sections are a good match to the observed V_P gradients, including the V_P minimum at the α-β quartz transition just above 20 km depth. In summary, the isotropic V_P observed for Qiangtang can be reasonably matched by some combination of marble, wacke, and tonalite; pelite and basalt could be present, but only in minor amounts.

6. Comparison of Calculated and Observed V_P/V_S and Poisson's Ratio

V_P/V_S can also be a good means by which to assess the composition of the crust, particularly because of the unusual elastic properties of quartz. The data set for V_P/V_S ratios from Qiangtang is relatively meager, however, and consists mostly of average values of 1.73–1.78 for the entire crust [*Owens and Zandt*, 1997; *Vergne et al*., 2002; *Jiang et al*., 2006; *Xu et al*., 2013a]; these values are more consistent with a quartz-dominated crust than a mafic crust, but only just (Figure 4). Figure 9 shows V_P/V_S for Qiangtang from *Mechie et al*. [2004]. The upper crust has such a low V_P/V_S (1.67) that it must contain quartz-rich rocks like the Funeral Mountains or the East Humboldt Range (about 35% and 45% quartz, respectively). The high V_P/V_S observed in the Qiangtang middle to lower crust (1.84) is similar to the carbonate-dominated Ruby Mountains section (only 11 vol % quartz in that section), similar to the basalt and tonalite model rocks and similar to the mafic Qiangtang xenoliths. The marked jump in observed V_P/V_S ratios at ~20 km depth is similar in magnitude to that produced by the α-β quartz transition for calculated V_P/V_S ratios. In summary, the isotropic V_P/V_S observed for Qiangtang can be reasonably matched by typical quartz-rich crustal rocks.

7. Petrology and Wave Speeds in Central Tibet Indicate a Partially Melted Mica-Bearing Crust

Comparison of observed and calculated V_P, V_S, and V_P/V_S for Qiangtang reveals that the wave speeds from Qiangtang are difficult to explain with melt-free and fluid-free crustal rock types. In particular—and

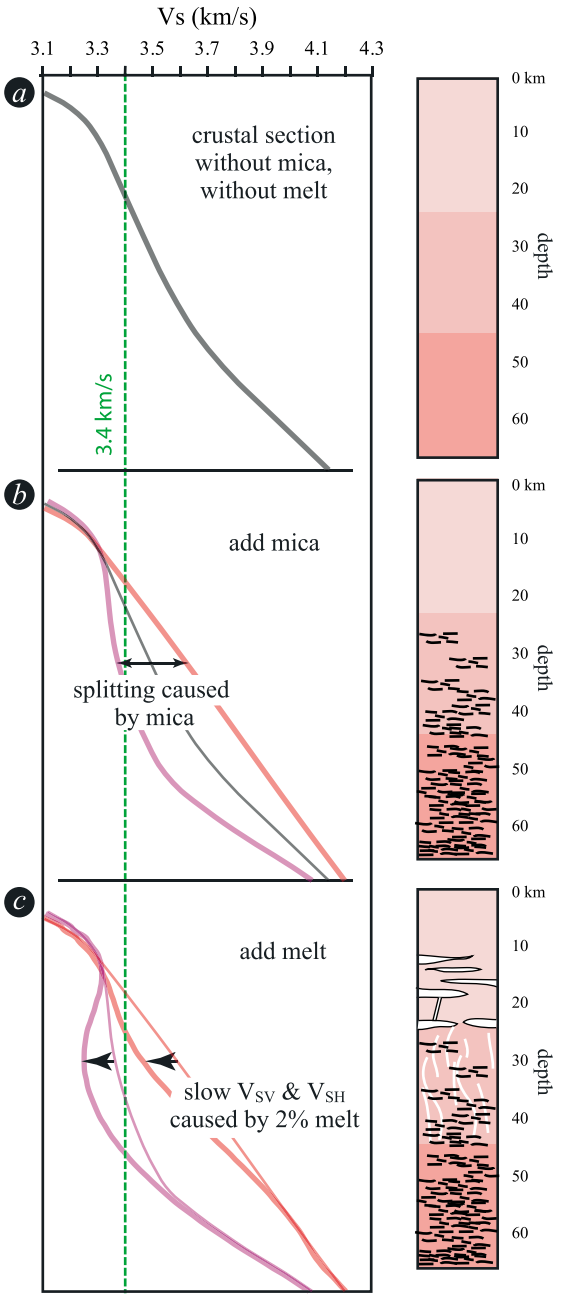

Figure 10. The observed radial anisotropy and slow V_S for Qiangtang can be explained by a subhorizontally foliated, mica-bearing crustal section with partial melt. (a) V_S for a hypothetical crustal section. (b) The addition of mica produces up to 10% radial anisotropy. (c) The addition of melt reduces the V_{SV} and V_{SH} to the slow speeds observed in the middle crust of the Tibetan Plateau.

remarkably—*none of the calculated wave speeds match the observed isotropic V_S and V_{SV} that are slower than 3.5 km/s*. This holds for (i) Tibetan xenoliths (Figure 7a), (ii) model rock types (Figure 7b), and (iii) Basin and Range crustal sections—and even includes anisotropy in the Basin and Range crustal sections (Figure 7c). Simply put, there is no reasonable solid isotropic or anisotropic geological material known to us that can explain the slow V_S and V_{SV} that are characteristic of the Qiangtang crust. Importantly, the slow speed is seen only in the V_{SV} determined from Rayleigh waves and not in the V_{SH} or Love wave component of radial anisotropy [*Shapiro et al.*, 2004].

The wave speeds and the radial anisotropy observed can be explained if the crust of Qiangtang contains a few percent partial melt and subhorizontally oriented mica. Imagine a 65 km thick crustal section in which V_S increases monotonically downward from ~3.1 km/s to ~4.1 km/s (Figure 10a). If this section contains subhorizontally oriented mica, the Basin and Range sections (Figure 7c) [*Erdman et al.*, 2013] tell us that V_{SV} can be less than V_{SH} by up to 10% (Figure 10b). For instance, at a depth of 25–35 km, V_{SV} might be ~3.35 km/s and V_{SH} might be 3.6 km/s (Figure 10b). Subhorizontally oriented mica in the Tibetan crust is exactly what is expected for a subhorizontally layered sedimentary section like that in Qiangtang. Even in the absence of deformation, the micas will be oriented subhorizontally. *Radial anisotropy is also, therefore, exactly what is expected in a sedimentary section, and may have no relevance to, or meaning for interpreting, strain within the plateau*.

Imagine now a small amount of partial melt within the Qiangtang middle crust. We seek to explain a reduction in V_{SV} at 25–35 km depth from ~3.35 km/s to 3.25 km/s (Figure 7)—i.e., a reduction of ~3%. Following *Schmeling* [1985], we calculate the effect of melt on V_S and V_P using the parameters in Table 4. For small melt fractions, all combinations of rocks and melts in Table 1 show similar reductions in wave speed for different melt geometries (Figure 11). A small amount of partial melt—less than 2% if the melt is in tubes—is sufficient to produce a 3% reduction in V_S. The effect on V_P is slightly smaller (Figure 11)—and that on V_P/V_S smaller still—and would enable a better correspondence between the observed and calculated V_P (Figure 8) and V_P/V_S (Figure 9).

Table 4. Physical Properties for Calculating the Effect of Melt on V_P and V_S[a]

Rock	ρ, Density (kg/m^3)	K, Bulk Modulus (GPa)	G, Shear Modulus (GPa)
Pelite	3170	107	60
Wacke	2890	81	42
Tonalite	3080	92	49
Andesite melt	2480	17	0
Rhyolite melt	2330	14	0

[a]The properties of rocks are for those in Table 1 at 1 GPa and 1000°C. The properties for melts are extrapolated to 1000°C and 1 atm using data in *Rivers and Carmichael* [1987]; it was assumed that ρ/K and ρ/G are identical at 1 atm and 1 GPa. (These approximations or even the rock type have little impact on the calculated % change in wave speed.)

8. Conclusions

The Qiangtang block of the central Tibetan Plateau is characterized by *S* wave speeds as slow as 3.3 km/s at depths from 20–25 km to 45–50 km. Satellite magnetic measurements, V_P/V_S ratios, and metamorphic temperatures of xenoliths suggest that the Qiangtang crust is hotter than the mica-dehydration solidi for crustal rocks at depths ≥20 km, permitting that the Qiangtang middle to lower crust is currently or formerly partially molten. The presence of 2% partial melt is sufficient to explain the slow observed *S* wave speeds.

The Qiangtang block is also characterized by *S* wave radial anisotropy of at least 4% ($V_{SH} > V_{SV}$) with stronger anisotropy in the west than the east; because estimates of radial anisotropy have been made assuming hexagonal symmetry with a vertical unique slow axis, the intrinsic anisotropy is likely to be higher. The presence of mica in Qiangtang xenoliths reinforces the fact that fluorine and titanium stabilize mica to temperatures well above the solidi, permitting that the Qiangtang lower crust, though currently or formerly partially molten, still contains mica. These micas, expected to be subhorizontally oriented either because of sedimentation or strain, are sufficient to explain the observed anisotropy. Thus, wave speeds and V_P/V_S ratios in the middle to deep crust of central Tibet are best explained by a partially melted, mica-bearing middle to lower crust with a subhorizontal to gently dipping foliation.

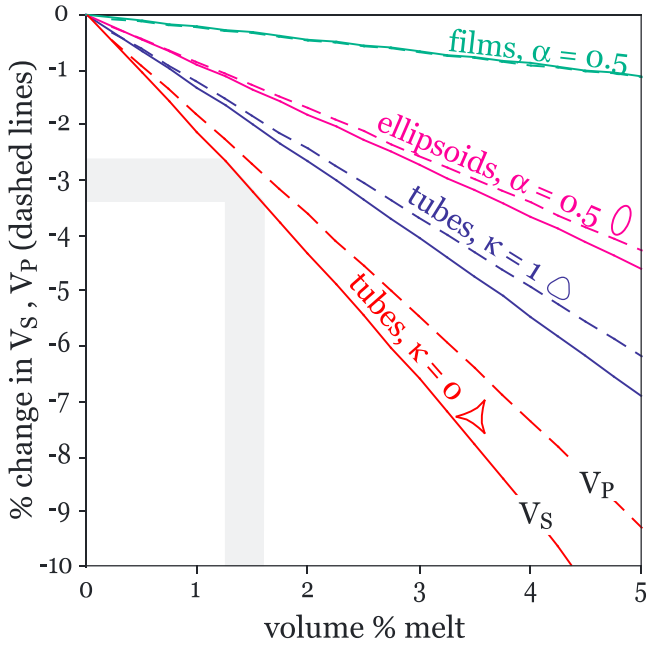

Figure 11. Effect of partial melt on V_S and V_P (dashed lines). The shapes of melt films, bubbles, and tubes are described by α and κ [after *Schmeling*, 1985].

Acknowledgments
Stéphane Guillot, an anonymous reviewer, and an anonymous Associate Editor provided helpful comments. John Cottle, Phil Gans, Roy Hyndman, Peter Kelemen, and Craig Manning provided helpful advice. Aspects of this work were supported at UCSB by NSF-EAR award 1008760 and at CU-Boulder by NSF-EAR awards 0944022 and EAR 1246925. The data used to produce the results of this paper are available from the authors on request.

References

Acton, C. E., K. Priestley, V. K. Gaur, and S. S. Rai (2010), Group velocity tomography of the Indo-Eurasian collision zone, *J. Geophys. Res.*, *115*, B12335, doi:10.1029/2009JB007021.

Aleksandrov, K. S., and T. V. Ryzhova (1961a), Elastic properties of rock-forming minerals. 1. Pyroxenes and amphiboles, *Bull. Acad. Sci. USSR, Geophys. Ser.*, *9*, 1165–1168.

Aleksandrov, K. S., and T. V. Ryzhova (1961b), Elastic properties of rock-forming minerals. II: Layered silicates, *Bull. Acad. Sci. USSR, Geophys. Ser.*, *12*, 871–875.

Aleksandrov, K. S., U. V. Alchikov, B. P. Belikov, B. I. Zaslavskii, and A. I. Krupni (1974), Velocities of elastic waves in minerals at atmospheric pressure and increasing precision of elastic constants by means of EVM, *Izvestiia Akademii nauk SSSR. Seriia geologicheskaia*, *10*, 15–24.

Alsdorf, D., and D. Nelson (1999), The Tibetan satellite magnetic low: Evidence for widespread melt in the Tibetan crust?, *Geology*, *27*, 943–946.

Auzanneau, E., M. W. Schmidt, D. Vielzeuf, and J. A. D. Connolly (2010), Titanium in phengite: A geobarometer for high temperature eclogites, *Contrib. Mineral. Petrol.*, *159*, 1–24.

Babuška, V., and M. Cara (1991), *Seismic Anisotropy in the Earth*, Modern approaches in geophysics, vol. 10, Kluwer Acad., Dordrecht.

Babuska, V., J. Fiala, M. Kumazawa, and I. Ohno (1978), Elastic properties of garnet solid-solution series, *Phys. Earth Planet. Inter.*, *16*, 157–176.

Bai, D., et al. (2010), Crustal deformation of the eastern Tibetan Plateau revealed by magnetotelluric imaging, *Nat. Geosci.*, *3*, 358–362, doi:10.1038/ngeo830.

Barth, N. C., B. R. Hacker, G. G. E. Seward, E. O. Walsh, D. Young, and S. Johnston (2010), Strain within the ultrahigh-pressure Western Gneiss region of Norway recorded by quartz CPOs, *Geol. Soc. London, Spec. Publ.*, *335*, 663–685, doi:10.1144/SP335.27.

Bensen, G. D., M. H. Ritzwoller, M. P. Barmin, A. L. Levshin, F. Lin, M. P. Moschetti, N. M. Shapiro, and Y. Yang (2007), Processing seismic ambient noise data to obtain reliable broad-band surface wave dispersion measurements, *Geophys. J. Int.*, *169*, 1239–1260, doi:10.1111/j.1365-246X.2007.03374.x.

Birch, F. (1961), The velocity of compressional waves in rocks to 10 kilobars: 2, *J. Geophys. Res.*, *66*, 2199–2224, doi:10.1029/JZ066i007p02199.

Bird, P. (1991), Lateral extrusion of lower crust from under high topography, in the isostatic limit, *J. Geophys. Res.*, *96*, 10,275–10,286, doi:10.1029/91JB00370.

Caldwell, W. B., S. L. Klemperer, S. S. Rai, and J. F. Lawrence (2009), Partial melt in the upper-middle crust of the northwest Himalaya revealed by Rayleigh wave dispersion, *Tectonophysics*, *477*, 58–65.

Chen, C. C., C. C. Lin, L. G. Liou, S. V. Sinogeikin, and J. D. Bass (2001), Elasticity of single-crystal calcite and rhodochrosite by Brillouin spectroscopy, *Am. Mineral.*, *86*, 1525–1529.

Chen, Y., J. Badal, and Z. Zhang (2009), Radial anisotropy in the crust and upper mantle beneath the Qinghai-Tibet Plateau and surrounding regions, *J. Asian Earth Sci.*, *36*, 289–302.

Chu, R., L. Zhu, and D. V. Helmberger (2009), Determination of earthquake focal depths and source time functions in central Asia using teleseismic P waveforms, *Geophys. Res. Lett.*, *36*, L17317, doi:10.1029/2009GL039494.

Chung, S.-L., M.-F. Chu, Y. Zhang, Y. Xie, C.-H. Lo, T.-Y. Lee, C.-Y. Lan, X. Li, Q. Zhang, and Y. Wang (2005), Tibetan tectonic evolution inferred from spatial and temporal variations in post-collisional magmatism, *Earth Sci. Rev.*, *68*, 173–196.

Clark, M. K., and L. H. Royden (2000), Topographic ooze: Building the eastern margin of Tibet by lower crustal flow, *Geology*, *28*, 703–706.

Coggon, R., and T. J. B. Holland (2002), Mixing properties of phengitic micas and revised garnet-phengite thermobarometers, *J. Metamorph. Geol.*, *20*, 683–696.

Connolly, J. A. D., and K. Petrini (2002), An automated strategy for calculation of phase diagram sections and retrieval of rock properties as a function of physical conditions, *J. Metamorph. Geol.*, *20*, 697–798.

Cotte, N., H. Pederson, M. Campillo, J. Mars, J. F. Ni, R. Kind, E. Sandvol, and W. Zhao (1999), Determination of the crustal structure in southern Tibet by dispersion and amplitude analysis of Rayleigh waves, *Geophys. J. Int.*, *138*, 809–819, doi:10.1046/j.1365-246x.1999.00927.x.

Craig, T. J., A. Copley, and J. Jackson (2012), Thermal and tectonic consequences of India underthrusting Tibet, *Earth Planet. Sci. Lett.*, *353–354*, 231–239.

DeCelles, P. G., D. M. Robinson, and G. Zandt (2002), Implications of shortening in the Himalayan fold-thrust belt for uplift of the Tibetan Plateau, *Tectonics*, *21*(6), 1062, doi:10.1029/2001TC001322.

Deng, W. (1996), Basic-ultrabasic and volcanic rocks in Chagbu-Shuanghu area of northern Xizang (Tibet), China, *Sci. China, Ser. D Earth Sci.*, *39*, 359–368.

Ding, L., P. Kapp, D. Zhong, and W. Deng (2003), Cenozoic volcanism in Tibet: Evidence for a transition from oceanic to continental subduction, *J. Petrol.*, *44*, 1833–1865.

Ding, L., P. Kapp, Y. Yue, and Q. Lai (2007), Postcollisional calc-alkaline lavas and xenoliths from the southern Qiangtang terrane, central Tibet, *Earth Planet. Sci. Lett.*, *254*, 28–38.

Dooley, D. F., and A. F. Patino Douce (1996), Fluid-absent melting of F-rich phlogopite + rutile + quartz, *Am. Mineral.*, *81*, 202–212.

Duret, F., N. M. Shapiro, Z. Cao, V. Levin, P. Molnar, and S. Roecker (2010), Surface wave dispersion across Tibet: Direct evidence for radial anisotropy in the crust, *Geophys. Res. Lett.*, *37*, L16306, doi:10.1029/2010GL043811.

Ebadi, A., and W. Johannes (1991), Beginning of melting and composition of first melts in the system Qz-Ab-Or-H2O-CO2, *Contrib. Mineral. Petrol.*, *106*, 286–295.

Erdman, M. E., B. R. Hacker, G. Zandt, and G. Seward (2013), Seismic anisotropy of the crust: Electron backscatter diffraction measurements from the Basin and Range, *Geophys. J. Int.*, *195*(2), doi:10.1093/gji/ggt287.

Fuhrman, M. L., and D. H. Lindsley (1988), Ternary-feldspar modeling and thermometry, *Am. Mineral.*, *73*, 201–215.

Galvé, A., A. Hirn, M. Jiang, J. Gallart, B. de Voogd, J.-C. Lepine, J. Diaz, Y. Wang, and H. Qian (2002), Modes of raising northeastern Tibet probed by explosion seismology, *Earth Planet. Sci. Lett.*, *203*, 35–43.

Galvé, A., M. Jiang, A. Hirn, M. Sapin, M. Laigle, B. de Voogd, J. Gallart, and H. Qian (2006), Explosion seismic P and S velocity and attenuation constraints on the lower crust of the North–Central Tibetan Plateau, and comparison with the Tethyan Himalayas: Implications on composition, mineralogy, temperature, and tectonic evolution, *Tectonophysics*, *412*, 141–157.

Guillot, S., and A. Replumaz (2013), Importance of continental subductions for the growth of the Tibetan plateau, *Bull. Soc. Geol. Fr.*, *184*, 199–223.

Guillot, S., P. Le Fort, A. Pêcher, M. R. Barman, and J. Aprahamian (1995), Contact metamorphism and depth of emplacement of the Manaslu granite (central Nepal). Implications for Himalayan orogenesis, *Tectonophysics*, *241*, 99–119.

Guo, Z., X. Gao, H. Yao, J. Li, and W. Want (2009), Midcrustal low velocity layer beneath the central Himalaya and southern Tibet revealed by ambient noise array tomography, *Geochem., Geophys., Geosyst.*, *10*, Q05007, doi:10.1029/2009GC002458.

Guynn, J. H., P. Kapp, A. Pullen, M. T. Heizler, G. Gehrels, and L. Ding (2006), Tibetan basement rocks near Amdo reveal "missing" Mesozoic tectonism along the Bangong suture, central Tibet, *Geology*, *34*, 505–508.

Hacker, B. R., and G. A. Abers (2004), Subduction Factory 3. An Excel worksheet and macro for calculating the densities, seismic wave speeds, and H2O contents of minerals and rocks at pressure and temperature, *Geochem., Geophys., Geosyst.*, *5*, Q01005, doi:10.1029/2003GC000614.
Hacker, B. R., E. Gnos, L. Ratschbacher, M. Grove, M. McWilliams, S. V. Sobolev, W. Jiang, and Z. Wu (2000), Hot and dry xenoliths from the lower crust of Tibet, *Science*, *287*, 2463–2466.
Hacker, B. R., P. B. Kelemen, and M. D. Behn (2011), Differentiation of the continental crust by relamination, *Earth Planet. Sci. Lett.*, *307*, 501–516.
Holland, T. J. B., and R. Powell (1998), An internally consistent thermodynamic data set for phases of petrological interest, *J. Metamorph. Geol.*, *16*, 309–343.
Holloway, J. R., and C. E. Ford (1975), Fluid-absent melting of the fluoro-hydroxy amphibole pargasite to 35 kilobars, *Earth Planet. Sci. Lett.*, *25*, 44–48.
Huang, H., H. Yao, and R. D. van der Hilst (2010), Radial anisotropy in the crust in SE Tibet and SW China from ambient noise interferometry, *Geophys. Res. Lett.*, *37*, L21310, doi:10.1029/2010GL044981.
Jiang, M., A. Galvé, A. Hirn, B. de Voogd, M. Laigle, H. P. Su, J. Diaz, J. C. Lepine, and Y. X. Wang (2006), Crustal thickening and variations in architecture from the Qaidam basin to the Qiang Tang (North–Central Tibetan Plateau) from wide-angle reflection seismology, *Tectonophysics*, *412*, 121–140.
Jiang, M., S. Zhou, E. Sandvol, X. Chen, X. Liang, Y. J. Chen, and W. Fan (2011), 3-D lithospheric structure beneath southern Tibet from Rayleigh wave tomography with a 2-D seismic array, *Geophys. J. Int.*, *185*, 593–608, doi:10.1111/j.1365-246X.2011.04979.x.
Kapp, P., A. Yin, C. E. Manning, T. M. Harrison, M. H. Taylor, and L. Ding (2003), Tectonic evolution of the early Mesozoic blueschist-bearing Qiangtang metamorphic belt, central Tibet, *Tectonics*, *22*(4), 1043, doi:10.1029/2002TC001383.
Kind, R., J. Ni, W. Zhao, J. Wu, X. Yuan, L. Zhao, E. Sandvol, C. Reese, J. Nabelek, and T. Hirn (1996), Evidence from earthquake data for a partially molten crustal layer in southern Tibet, *Science*, *274*, 1692–1694.
Lakshtanov, D. L., S. V. Sinogeikin, and J. D. Bass (2007), High-temperature phase transitions and elasticity of silica polymorphs, *Phys. Chem. Miner.*, *34*, 11–22.
LeFort, P. (1981), Manaslu leucogranite: A collision signature of the Himalaya. A model for its genesis and emplacement, *J. Geophys. Res.*, *86*, 10,545–10,568, doi:10.1029/JB086iB11p10545.
Levshin, A. L., X. Yang, M. P. Barmin, and M. H. Ritzwoller (2010), Midperiod Rayleigh wave attenuation model for Asia, *Geochem., Geophys., Geosyst.*, *11*, Q08017, doi:10.1029/2010GC003164.
Li, H., W. Su, C.-Y. Wang, and Z. Huang (2009), Ambient noise Rayleigh wave tomography in western Sichuan and eastern Tibet, *Earth Planet. Sci. Lett.*, *282*, 201–211, doi:10.1016/j.epsl.2009.03.021.
Li, Y. H., Q. J. Wu, X. B. Tian, R. S. Zeng, R. Q. Zhang, and H. G. Li (2006), Crustal structure beneath Qiangtang and Lhasa terrane from receiver function, *Acta Seismol. Sin.*, *19*, 633–642.
Liang, C., and X. Song (2006), A low velocity belt beneath northern and eastern Tibetan Plateau from Pn tomography, *Geophys. Res. Lett.*, *33*, L22306, doi:10.1029/2006GL027926.
Makovsky, Y., and S. Klemperer (1999), Measuring the seismic properties of Tibetan bright spots: Evidence for free aqueous fluids in the Tibetan middle crust, *J. Geophys. Res.*, *104*, 10,795–10,825, doi:10.1029/1998JB900074.
Makovsky, Y., S. Klemperer, and L. Ratschbacher (1999), Midcrustal reflector on INDEPTH wide-angle profiles: An ophiolitic slab beneath the India–Asia suture in southern Tibet?, *Tectonics*, *18*, 793–808, doi:10.1029/1999TC900022.
McNamara, D. E., W. R. Walter, T. J. Owens, and C. J. Ammon (1997), Upper mantle velocity structure beneath the Tibetan Plateau from Pn travel time tomography, *J. Geophys. Res.*, *102*, 493–505, doi:10.1029/96JB02112.
Mechie, J., S. V. Sobolev, L. Ratschbacher, A. Y. Babeyko, G. Bock, A. G. Jones, K. D. Nelson, K. D. Solon, L. D. Brown, and W. Zhao (2004), Precise temperature estimation in the Tibetan crust from seismic detection of the a-b quartz transition, *Geology*, *32*, 601–604.
Montel, J. M., and D. Vielzeuf (1997), Partial melting of metagreywackes, Part II. Compositions of minerals and melts, *Contrib. Mineral. Petrol.*, *128*, 176–196.
Nichols, G. T., P. J. Wyllie, and C. R. Stern (1994), Subduction zone melting of pelagic sediments constrained by melting experiments, *Nature*, *371*, 785–788.
Ohno, I., K. Harada, and C. Yoshitomi (2006), Temperature variation of elastic constants of quartz across the α-β transition, *Phys. Chem. Miner.*, *33*, 1–9.
Owens, T. J., and G. Zandt (1997), Implications of crustal property variations for models of Tibetan plateau evolution, *Nature*, *387*, 37–43.
Patiño Douce, A. E. (2005), Vapor-absent melting of tonalite at 15–32 kbar, *J. Petrol.*, *46*, 275–290.
Patiño Douce, A. E., and J. S. Beard (1995), Dehydration-melting of biotite gneiss and quartz amphibolite from 3 to 15 kbar, *J. Petrol.*, *36*, 707–738.
Patiño Douce, A. E., and T. C. McCarthy (1998), Melting of crustal rocks during continental collision and subduction, in *When Continents Collide: Geodynamics and Geochemistry of Ultrahigh-Pressure Rocks*, edited by B. R. Hacker and J. G. Liou, pp. 27–55, Kluwer Acad., Dordrecht.
Pullen, A., P. Kapp, G. E. Gehrels, L. Ding, and Q. Zhang (2010), Metamorphic rocks in central Tibet: Lateral variations and implications for crustal structure, *Geol. Soc. Am. Bull.*, doi:10.1130/B30154.1.
Rai, S. S., A. Ashish, A. Padhi, and P. R. Sarma (2009), High crustal seismic attenuation in Ladakh-Karakoram, *Bull. Seismol. Soc. Am.*, *99*, 407–415, doi:10.1785/0120070261.
Rapine, R., F. Tilmann, M. West, and J. Ni (2003), Crustal structure of northern and southern Tibet from surface wave dispersion analysis, *J. Geophys. Res.*, *108*(2), 2120, doi:10.1029/2001JB000445.
Rapp, R. P., and E. B. Watson (1995), Dehydration melting of metabasalt at 8–32 kbar: Implications for continental growth and crust-mantle recycling, *J. Petrol.*, *36*, 893–931.
Rivers, M. L., and I. S. E. Carmichael (1987), Ultrasonic studies of silicate melts, *J. Geophys. Res.*, *92*, 9247–9270, doi:10.1029/JB092iB09p09247.
Scaillet, B., and M. P. Searle (2006), Mechanisms and timescales of felsic magma segregation, ascent and emplacement in the Himalaya, *Geol. Soc. London, Spec. Publ.*, *268*, 293–308.
Schmeling, H. (1985), Numerical models on the influence of partial melt on elastic, anelastic and electric properties of rocks, Part I: Elasticity and anelasticity, *Phys. Earth Planet. Inter.*, *41*, 34–57.
Schmidt, J., B. R. Hacker, L. Ratschbacher, K. Stübner, M. Stearns, A. Kylander-Clark, J. M. Cottle, A. A. G. Webb, G. Gehrels, and V. Minaev (2011), Cenozoic deep crust in the Pamir, *Earth Planet. Sci. Lett.*, *312*, 411–421.
Schwab, M., et al. (2004), Assembly of the Pamirs: Age and origin of magmatic belts from the southern Tien Shan to the southern Pamirs and their relation to Tibet, *Tectonics*, *23*, TC4002, doi:10.1029/2003TC001583.
Searle, M. P. (1999), Emplacement of Himalayan leucogranites by magma injection along giant sill complexes: Examples from the Cho Oyu, Gyachung Kang and Everest leucogranites (Nepal Himalaya), *J. Asian Earth Sci.*, *17*, 773–783.

Searle, M. P., J. M. Cottle, M. J. Streule, and D. J. Waters (2010), Crustal melt granites and migmatites along the Himalaya: Melt source, segregation, transport and granite emplacement mechanisms, *Trans. R. Soc. Edinburgh: Earth Sci.*, *100*, 219–233.
Sen, C., and T. Dunn (1994), Dehydration melting of a basaltic compositions amphibolite at 1.5 and 2.0 GPa: Implications for the origin of adakites, *Contrib. Mineral. Petrol.*, *117*, 394–409.
Shapiro, N. M., and M. H. Ritzwoller (2002), Monte-Carlo inversion for a global shear velocity model of the crust and upper mantle, *Geophys. J. Int.*, *151*, 88–105, doi:10.1046/j.1365-246X.2002.01742.x.
Shapiro, N. M., M. H. Ritzwoller, P. Molnar, and V. Levin (2004), Thinning and flow of Tibetan crust constrained by seismic anisotropy, *Science*, *305*, 233–236.
Skjerlie, K. P., and A. D. Johnston (1993), Fluid-absent melting behavior of an F-rich tonalitic gneiss at mid-crustal pressures: Implications for the generation of anorogenic granites, *J. Petrol.*, *34*, 785–815.
Sloan, R. A., J. A. Jackson, D. McKenzie, and K. Priestley (2011), Earthquake depth distributions in central Asia, and their relations with lithospheric thickness, shortening and extension, *Geophys. J. Int.*, *185*, 1–29, doi:10.1111/j.1365-246X.2010.04882.x.
Tajcmanová, L., J. A. D. Connolly, and B. Cesare (2009), A thermodynamic model for titanium and ferric iron solution in biotite, *J. Metamorph. Geol.*, *27*, 153–164.
Thompson, J. B., and G. L. Hovis (1979), Entropy of mixing in sanidine, *Am. Mineral.*, *64*, 57–65.
Turner, S., N. Arnaud, J. Liu, N. Rogers, C. Hawkesworth, N. Harris, S. Kelley, P. Van Calsteren, and W. Deng (1996), Post-collision, shoshonitic volcanism on the Tibetan Plateau: Implications for convective thinning of the lithosphere and the source of ocean island basalts, *J. Petrol.*, *37*, 45–71.
Unsworth, M. J., A. G. Jones, W. Wei, G. Marquis, S. G. Gokarn, J. E. Spratt, and I.-M. Team (2005), Crustal rheology of the Himalaya and Southern Tibet inferred from magnetotelluric data, *Nature*, *483*, 78–81.
Vaughan, M., and S. Guggenheim (1986), Elasticity of muscovite and its relationship to crystal structure, *J. Geophys. Res.*, *91*, 4657–4664, doi:10.1029/JB091iB05p04657.
Vergne, J., G. Wittlinger, H. Qiang, P. Tapponnier, G. Poupinet, M. Jiang, G. Herquel, and A. Paul (2002), Seismic evidence for stepwise thickening of the crust across the NE Tibetan Plateau, *Earth Planet. Sci. Lett.*, *203*, 25–33.
Vielzeuf, D., and J. M. Montel (1994), Partial melting of metagreywackes. 1. Fluid-absent experiments and phase relationships, *Contrib. Mineral. Petrol.*, *117*, 375–393.
Vielzeuf, D., and J. R. Holloway (1988), Experimental determination of the fluid-absent melting relations in the pelitic system. Consequences for crustal differentiation, *Contrib. Mineral. Petrol.*, *98*, 257–76.
Villaseñor, A., M. H. Ritzwoller, A. L. Levshin, M. P. Barmin, E. R. Engdahl, W. Spakman, and J. Trampert (2001), Shear velocity structure of central Eurasia from inversion of surface wave velocities, *Phys. Earth Planet. Inter.*, *123*, 169–184, doi:10.1016/S0031-9201(00)00208-9.
Wang, Q., S.-L. Chung, X.-H. Li, D. Wyman, Z.-X. Li, W.-D. Sun, H.-N. Qiu, Y.-S. Liu, and Y.-T. Zhu (2012), Crustal melting and flow beneath Northern Tibet: Evidence from Mid-Miocene to Quaternary strongly peraluminous rhyolites in the Southern Kunlun Range, *J. Petrol.*, doi:10.1093/petrology/egs058.
Wang, Y., W. D. Mooney, X. Yuan, and N. Okaya (2013), Crustal structure of the northeastern Tibetan Plateau from the Southern Tarim Basin to the Sichuan Basin, China, *Tectonophysics*, *584*, 191–208.
Wei, C., and R. Powell (2003), Phase relations in high-pressure metapelites in the system KFMASH (K2O-FeO-MgO-Al2O3-SiO2-H2O) with application to natural rocks, *Contrib. Mineral. Petrol.*, *145*, 301–315.
White, R. W., R. Powell, T. J. B. Holland, and B. Worley (2000), The effect of TiO2 and Fe2O3 on metapelitic assemblages at greenschist and amphibolite facies conditions: Mineral equilibria calculations in the system K2O-FeO-MgO-Al2O3-SiO2-H2O-TiO2-Fe2O3, *J. Metamorph. Geol.*, *18*, 497–511.
Xie, J. (2004), Lateral variations of crustal seismic attenuation along the INDEPTH profiles in Tibet from Lg Q inversion, *J. Geophys. Res.*, *109*, B10308, doi:10.1029/2004JB002988.
Xie, J., M. H. Ritzwoller, W. Shen, Y. Yang, Y. Zheng, and L. Zhou (2013), Crustal radial anisotropy across eastern Tibet and the western Yangtze craton, *J. Geophys. Res. Solid Earth*, *118*, 4226–4252, doi:10.1002/jgrb.50296.
Xu, L., S. Rondenay, and R. D. van der Hilst (2007), Structure of the crust beneath the southeastern Tibetan Plateau from teleseismic receiver functions, *Phys. Earth Planet. Inter.*, *165*, 176–193, doi:10.1016/j.pepi.2007.09.002.
Xu, Q., J. Zhao, S. Pei, and H. Liu (2013a), Distinct lateral contrast of the crustal and upper mantle structure beneath northeast Tibetan plateau from receiver function analysis, *Phys. Earth Planet. Inter.*, *217*, 1–9.
Xu, Z. J., X. Song, and L. Zhu (2013b), Crustal and uppermost mantle S velocity structure under Hi-CLIMB seismic array in central Tibetan Plateau from joint inversion of surface wave dispersion and receiver function data, *Tectonophysics*, *584*, 209–220.
Yang, Y., et al. (2010), Rayleigh wave phase velocity maps of Tibet and the surrounding regions from ambient seismic noise tomography, *Geochem., Geophys., Geosyst.*, *11*, Q08010, doi:10.1029/2010GC003119.
Yang, Y., M. H. Ritzwoller, Y. Zheng, W. Shen, A. L. Levshin, and Z. Xie (2012), A synoptic view of the distribution and connectivity of the mid-crustal low velocity zone beneath Tibet, *J. Geophys. Res.*, *117*, B04303, doi:10.1029/2011JB008810.
Yao, H., C. Beghein, and R. D. van der Hilst (2008), Surface wave array tomography in SE Tibet from ambient seismic noise and two-station analysis: II. Crustal and upper-mantle structure, *Geophys. J. Int.*, *173*, 205–219, doi:10.1111/j.1365-246X.2007.03696.x.
Yao, H., R. D. van der Hilst, and J.-P. Montagner (2010), Heterogeneity and anisotropy of the lithosphere of SE Tibet from surface wave array tomography, *J. Geophys. Res.*, *115*, B12307, doi:10.1029/2009JB007142.
Yin, A., and T. M. Harrison (2000), Geologic evolution of the Himalayan–Tibetan orogen, *Annu. Rev. Earth Planet. Sci.*, *28*, 211–280.